Energy & Environmental Science

RSC Publishing

PAPER

View Article Online
View Journal | View Issue

Cite this: *Energy Environ. Sci.*, 2013, **6**, 2664

Controlled synthesis of hierarchical $Co_xMn_{3-x}O_4$ array micro-/nanostructures with tunable morphology and composition as integrated electrodes for lithium-ion batteries†

Le Yu, Lei Zhang, Hao Bin Wu, Genqiang Zhang and Xiong Wen (David) Lou*

Received 7th April 2013
Accepted 19th June 2013

DOI: 10.1039/c3ee41181h

www.rsc.org/ees

Hierarchical $Co_xMn_{3-x}O_4$ array micro-/nanostructures with tunable morphology and composition have been grown on conductive stainless steel with robust adhesion by a facile solvothermal route and a subsequent annealing treatment. By simply controlling the volume ratio of components in the mixed solvent, the morphology of the products can be tailored from hierarchical nanowires to nanosheets. Benefitting from the unique structural features, the resultant $CoMn_2O_4$ nanowires and $MnCo_2O_4$ nanosheets exhibit excellent electrochemical performance with remarkable specific capacities (540–207 mA h g^{-1}) at various current rates (1–10 C) and good cycling stability for highly reversible lithium storage. The enhanced electrochemical performance suggests their promising use as integrated binder-free electrodes for microscale lithium-ion batteries.

Broader context

Rechargeable lithium-ion batteries (LIBs) with higher energy/power density are the dominant power sources for numerous portable consumer electronic devices with a market value of billions of dollars. The employment of electrode materials with micro-/nanostructures has been regarded as an effective strategy for developing high-performance LIBs. In particular, an emerging new concept is to grow electroactive nanostructures on conductive substrates to form integrated three-dimensional (3D) electrodes to boost the electrochemical performance. In this contribution, we have rationally designed hierarchical $Co_xMn_{3-x}O_4$ array micro-/nanostructures with tunable morphology and composition as integrated electrodes for highly reversible lithium storage.

Introduction

Rechargeable lithium-ion batteries (LIBs) are the dominant power sources for numerous portable consumer electronic devices due to their advantages such as high energy density, long lifespan and environmental benignity.[1–8] However, conventional bulk electrode materials are approaching their inherent limits in performance and could hardly fulfil the ever-growing demands for the large-scale energy applications such as electric vehicles (EVs), and hybrid electric vehicles (HEVs).[9] The research and development of new attractive electrode materials have become the essential part of the current endeavour to boost the electrochemical performance of LIBs.[10–12]

Amongst the available materials, $Co_xMn_{3-x}O_4$ mixed oxides have attracted increasing attention as potential anode materials for next-generation LIBs, owing to their favourable characteristics inherited from Mn-based and Co-based metal oxides.[13–18] Interestingly, $Co_xMn_{3-x}O_4$ can store Li^+ ions based on a redox conversion reaction, where the metal oxide is reduced to metallic (Mn and Co) nanocrystals dispersed in a Li_2O matrix upon lithiation which are then reversibly restored to corresponding oxides after delithiation, leading to higher reversible theoretical capacities than that of commercial carbonaceous materials (372 mA h g^{-1}) as anode materials.[14,19] Co-based metal oxides such as CoO can deliver as much as two times the capacity of currently used graphite.[20,21] Meanwhile, Mn-based oxides possess lower operating voltages for lithium extraction. Besides, manganese is more abundant in nature and relatively low-cost (20 times cheaper than cobalt).[22,23] In addition, superior to single-phase oxides, mixed metal oxides can synergistically enhance the electrochemical properties such as electrical/ionic conductivity, reversible capacity, and mechanical stability.[18,24–26] Nonetheless, bulk Co-based and Mn-based metal oxides often suffer from short calendar life and/or poor rate capability. These problems have long been partly attributed to the pronounced volume variations (>200%) upon the repetitive lithium uptake and removal reactions, which generate local stress and eventually result in severe disintegration/pulverization of the electrode and hence a loss of electrical contacts between adjacent particles.[5]

School of Chemical and Biomedical Engineering, Nanyang Technological University, 62 Nanyang Drive, Singapore, 637459, Singapore. E-mail: xwlou@ntu.edu.sg; Web: http://www.ntu.edu.sg/home/xwlou/

† Electronic supplementary information (ESI) available. See DOI: 10.1039/c3ee41181h

One of the effective strategies to prolong the cycling lifespan is to tailor the particle size of electroactive materials to the nanometer-scale.[9,27–30] Nanosized structures endow the metal oxides with a shorter Li^+ ion diffusion path and increased specific surface area for good penetration of the electrolyte, leading to enhanced rate capability. However, nanometer-sized particles with high surface energy undergo pronounced agglomeration upon electrochemical cycling. Moreover, high surface area has been demonstrated to raise the risk of secondary reactions involving electrolyte decomposition between the electrode and the electrolyte, which gives rise to irreversible capacity and poor cycling performance. To solve the above problem, the employment of electrode materials with micro-/nano-structures has been regarded as an effective strategy for developing high-performance LIBs because the hierarchical structures might inherit the advantages from both the nanosized building blocks and microsized assemblies with negligible diffusion length and good cycling stability.[29,31,32] Recently, a few studies have reported the syntheses of hierarchical $Co_xMn_{3-x}O_4$ micro-/nanostructures and evaluated their electrochemical properties as negative electrodes for LIBs with encouraging results. For example, Chen and coworkers reported the fabrication of hierarchical $CoMn_2O_4$ microspheres assembled with porous nanosheets, which show a high discharge capacity of 894 mA h g^{-1} at a current density of 100 mA g^{-1} after 65 cycles.[19] Double-shelled $CoMn_2O_4$ hollow microcubes composed of nanometer-sized primary particles can retain a reversible capacity of 624 mA h g^{-1} at a current density of 200 mA g^{-1} after 50 cycles.[14] Xiong and coworkers synthesized the $Mn_{1.5}Co_{1.5}O_4$ core–shell microspheres with nanosized or submicrometer sized building blocks, which deliver a capacity of about of 618 mA h g^{-1} at a current density of 400 mA g^{-1} even after 300 cycles.[16] Besides, Xiong and coworkers recently synthesized multiporous $MnCo_2O_4$ and $CoMn_2O_4$ spinel quasi-hollow spheres with a tunable pore size and a quasi-hollow interior through a facile solvothermal route. The resultant $MnCo_2O_4$ samples could deliver a capacity of 610 mA h g^{-1} at a current density of 400 mA g^{-1} with good capacity retention after 100 cycles.[17]

Notwithstanding the above advances, synthesis of hierarchical $Co_xMn_{3-x}O_4$ micro-/nanostructures is still quite limited so far. In addition, current $Co_xMn_{3-x}O_4$ based anode materials need to be combined with polymeric binders and conductive agents during the electrode preparation. This will add an undesirable interface and inactive weight to the electrode, which inevitably compromises the overall energy storage capacity.[33] On the other hand, an emerging new concept is to grow electroactive nanostructures on conductive substrates to form integrated three-dimensional (3D) electrodes.[34–37] Furthermore, such integrated 3D nanoarrays can also serve as the pathway for efficient electron transport.[36,38] However, until now, the direct growth of free-standing and well-assembled hierarchical $Co_xMn_{3-x}O_4$ structures on current-collecting substrates has not been realized.

Based on the above considerations, we develop a facile solvothermal method to fabricate arrays of Co–Mn precursor based hierarchical structures on a stainless steel substrate, which are then converted into porous $Co_xMn_{3-x}O_4$ counterparts *via* a post-annealing treatment. By controlling the composition of the mixed solvent used for the solvothermal reaction, the structure of the products can be tailored from hierarchical nanowires to nanosheets. Meanwhile, the molar ratio of Mn to Co can be tuned from 2 : 1 to 1 : 2 within the final product. The as-formed hierarchical structures of porous $CoMn_2O_4$ nanowires and $MnCo_2O_4$ nanosheets are in good contact with the substrate and therefore could be directly used as the integrated electrodes without any ancillary materials. Remarkably, the as-synthesized 3D hierarchical structures of $CoMn_2O_4$ nanowires and $MnCo_2O_4$ nanosheets manifest promising electrochemical performance as electrodes for LIBs.

Experimental

Synthesis of hierarchical $Co_xMn_{3-x}O_4$ micro-/nanostructures on stainless steel or Ti foil

All the chemicals were of analytical grade and were used without further purification. In a typical synthesis, stainless steel foil or Ti foil (2 cm × 7 cm in rectangular shape) was immersed in a 3 M HCl solution for 15 min to eliminate the possible surface oxide layer before reaction. 1 mmol of $Co(NO_3)_2 \cdot 6H_2O$ and 2 mmol of $MnSO_4 \cdot H_2O$ were dissolved into a mixed solvent of ethanol (10 mL) and DI water (70 mL) at room temperature to form a clear pink solution (total solution volume is 80 mL), followed by the addition of 12 mmol of urea. In order to control the morphology of the precursor, the amount of ethanol was varied in the range of 0–70 mL keeping the total volume of 80 mL. The solution was then transferred to a capped bottle, and the pretreated stainless steel foil or Ti foil was placed in the bottle. Afterwards, the bottle was heated to 90 °C in an electric oven. After reaction for 6 h, the substrate was taken out and then cleaned by ultrasonication to remove the loosely attached products on the surface before being fully dried in air at 60 °C for further characterization. In order to get crystallized $Co_xMn_{3-x}O_4$ nanostructures, the conductive substrates with the as-grown precursor hierarchical structures were annealed in air at 600 °C with a temperate ramp rate of 1 °C min^{-1} for 4 h. It is interesting to note that this annealing step will not cause the formation of iron oxides. On average, the mass loading of the $Co_xMn_{3-x}O_4$ nanostructures is about 0.38 mg on 1 cm × 1 cm of stainless steel foil, carefully weighed after calcination.

Materials characterization

The morphology of the samples was characterized by a field-emission scanning electron microscope (FESEM; JEOL-6700) and a transmission electron microscope (TEM; JEOL, JEM-2010). The composition of the samples was analyzed by an energy-dispersive X-ray spectroscope (EDX) attached to the FESEM instrument. The crystal phase of the products was examined on a Bruker D2 Phaser X-ray diffractometer with Ni filtered Cu Kα radiation ($\lambda = 1.5406$ Å) at a voltage of 30 kV and a current of 10 mA. X-ray photoelectron spectroscope (XPS) measurements were performed on a VG ESCALAB MKII X-ray photoelectron spectrometer. All of the binding energies (BEs) in this XPS analysis were corrected for specimen charging by

referencing them to the C 1s peak (set at 284.6 eV). The nitrogen sorption measurement was performed on an Autosorb 6B at liquid-nitrogen temperature.

Electrochemical measurements

Electrochemical measurements were carried out using two-electrode Swagelok-type cells with pure lithium foil as the counter and reference electrodes at room temperature. The stainless steel foil supported hierarchical $Co_xMn_{3-x}O_4$ structures were directly applied as the working electrodes without an ancillary binder or conductive agent. The electrolyte was 1.0 M $LiPF_6$ in a 50 : 50 (w/w) mixture of ethylene carbonate and diethyl carbonate. Cell assembly was carried out in an Ar-filled glovebox with both moisture and oxygen concentrations below 1.0 ppm. The galvanostatic charging–discharging tests were performed on a NEWARE battery tester with a cut-off voltage window of 0.05–3.0 V *vs.* Li^+/Li. Electrochemical impedance spectroscopy (EIS) measurements were carried out on a CHI 660D electrochemical workstation by applying an AC voltage with 1 mV amplitude in a frequency range from 0.1 Hz to 100 kHz.

Results and discussion

Synthesis and structural analysis

In the present synthesis strategy, two steps are involved: the urea assisted solvothermal process to fabricate arrays of Co–Mn precursor based hierarchical structures on the stainless steel substrate and then a post-calcination treatment to generate the corresponding hierarchical structured $Co_xMn_{3-x}O_4$. The detailed preparation procedure can be found in the Experimental section. The morphologies of the Co–Mn precursor are first characterized by a field-emission scanning electron microscope (FESEM), as shown in Fig. 1. As the supersaturation for nucleation and crystal growth is determined by the solvent polarity and solubility, the morphology of Co–Mn precursor nanostructures can be readily controlled by adjusting the volumetric ratio of ethanol/water in the mixed solvent. When the reaction solvent is pure water, one-dimensional (1D) Co–Mn precursor structures (denoted as CMO-0) with a wire-like shape are uniformly grown on the substrate to form a uniform array over a large area (Fig. 1a). Interestingly, from the enlarged top-view and transmission electron microscope (TEM) image of CMO-0 (Fig. S1, see the ESI†), it can be observed that the hierarchical nanowires are composed of secondary bundle subunits with clear texture, the diameter of the tip is about 50 to 100 nm. The introduction of ethanol leads to the formation of large nanosheet structures on the substrate. When the volumetric ratio of ethanol/water reaches 30/50, as displayed in Fig. 1b, nanowires still exist and some even cover the surface of nanosheets. If the solvent is obtained by mixing equal volumes of ethanol and water, more nanosheets are found in the product and they interconnect with each other to form a dense wall-like structure with no nanowires attached (Fig. 1c). With the further increase of ethanol in the mixed solvent (v/v = 50/30), the nanosheets become even larger in size compared to those in CMO-40, producing an ordered array with a highly open and porous structure (Fig. 1d). As illustrated in Fig. S2,† the nanosheets exhibit a smooth surface with some cracks at the edge, the thickness of which is about 100 nm. Due to the low solubility of $MnSO_4$ in ethanol, a translucent pink sol instead of a clear solution is produced after the precursor chemicals are dissolved in the mixed solvent with less water (v/v = 60/20 and 70/10). After the solvothermal reaction, the resulting CMO-60 product possesses a sheet-like structure with loose connection, while the CMO-70 sample owns a nanosheet structure with

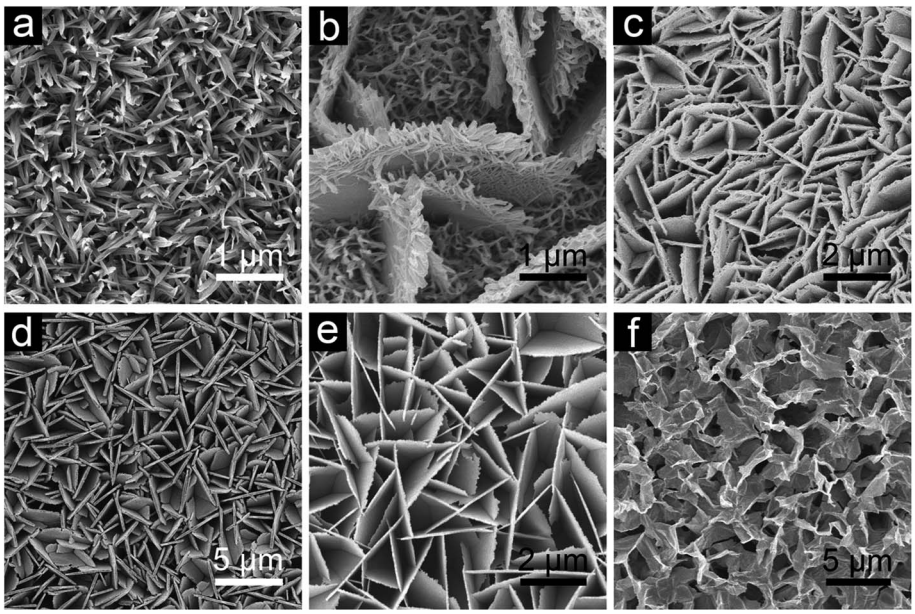

Fig. 1 FESEM images of Co–Mn precursor structures grown on stainless steel foil with different ethanol/water volume ratios: (a) CMO-0, v(EtOH/H_2O) = 0/80 mL; (b) CMO-30, v(EtOH/H_2O) = 30/50 mL; (c) CMO-40, v(EtOH/H_2O) = 40/40 mL; (d) CMO-50, v(EtOH/H_2O) = 50/30 mL; (e) CMO-60, v(EtOH/H_2O) = 60/20 mL and (f) CMO-70, v(EtOH/H_2O) = 70/10 mL.

rippled silk morphology due to its ultrathin feature. X-ray diffraction (XRD) analysis confirms that these Co–Mn precursor nanostructures can be mainly assigned to Co–Mn carbonate or oxide hydrate (Fig. S3, see ESI†). Similar nanostructures are obtained using Ti foil as the substrate or in the absence of a substrate, indicating the versatility of the present system (Fig. S4, see ESI†).

In addition to the solvent composition, the relative amount of Co and Mn precursor chemicals in the reaction solution will also have a significant effect on the hierarchical structures of the products (Fig. S5, see ESI†). Without the Mn salt, the resulting Co-based structures are composed of needles and sheets if water is used as the solvent or pure needle-like nanostructures with a smooth surface in the mixed solvent. In sharp contrast, the Mn-based product structures can hardly grow on the stainless steel. Only some irregular octahedra-like or bud-like particles can be found on the surface.

Based on previous investigation on the related $Co_xMn_{3-x}O_4$ structures, we chose 600 °C as the calcination temperature for the final composite oxides.[14,18,19] For the convenience of the discussion, we focus on two mixed oxides obtained from CMO-0 and CMO-50 as the representative products for the hierarchical structures of nanowires and nanosheets. The obtained oxides are first analyzed by XRD to determine their crystallographic structures. As reported in Fig. 2, the hierarchical $Co_xMn_{3-x}O_4$ structures are scratched from the substrate to avoid the impact of the stainless steel substrate on the XRD results. All of the reflections of hierarchical nanowires obtained by calcining CMO-0 could be assigned to body-centered-tetragonal $CoMn_2O_4$ (JCPDS card no. 77-0471, space group: $I4_1/amd$, $a = b = 5.784$ Å, $c = 9.091$ Å, $\alpha = \beta = \gamma = 90°$) without noticeable signals of residues or contaminants.[18] The energy-dispersive X-ray spectroscopy (EDX) result (Fig. S6, see ESI†) indicates that the Co/Mn atomic ratio of the hierarchical nanowire structure is about 1 : 2.03, which perfectly agrees with the theoretical value. Whereas, the XRD pattern for the nanosheet structure derived from CMO-50 confirms the formation of the face-centered-cubic $MnCo_2O_4$ phase (JCPDS card no. 23-1237, space group: $Fd3m$, $a = b = c = 8.269$ Å, $\alpha = \beta = \gamma = 90°$).[18] Both the phases adopt a distorted spinel structure, in which Mn and Co ions are distributed over octahedral and tetrahedral stacking interstices. The crystallite sizes of $CoMn_2O_4$ and $MnCo_2O_4$ nanostructures determined using the Scherrer equation are about 26.0 nm and 15.5 nm, respectively, which indicates that the $Co_xMn_{3-x}O_4$ samples are composed of nanocrystalline subunits, consistent with the TEM observation. Meanwhile, the elemental composition of the nanosheet structure characterized by EDX shows a Co/Mn atomic ratio of 1.84 : 1 (Fig. S6, see ESI†), although the precursor salt concentrations of Co and Mn are the same in the synthesis of CMO-0 and CMO-50. One might speculate that compared to Co^{2+} ions it is more difficult for Mn^{2+} ions to precipitate in an ethanol dominant mixed solvent. X-ray photoelectron (XPS) measurement suggests the co-existence of Mn^{2+}/Mn^{3+} and Co^{2+}/Co^{3+} cations in both the $CoMn_2O_4$ and $MnCo_2O_4$ samples (Fig. S7, see ESI†).

FESEM and TEM studies provide further insights into the morphologies and detailed geometrical structures of the as-prepared hierarchical structures of $Co_xMn_{3-x}O_4$. As depicted in Fig. 3, after the annealing treatment with a slow heating rate of 1 °C min^{-1}, the overall morphologies of these Co–Mn precursors can be well preserved within the crystalline $Co_xMn_{3-x}O_4$ structures without significant aggregation or collapse. The hierarchical $CoMn_2O_4$ nanowires inherit 1D features from the precursor with a similar diameter and length, except for a rougher exterior. As elucidated by TEM observation in Fig. 3c, each $CoMn_2O_4$ nanowire is composed of numerous primary nanoparticles with a size of tens of nanometers. As determined by N_2 sorption measurement at 77 K (Fig. S8, see ESI†), the open pores formed by the arrays and small mesopores between the nanometer-sized building blocks endow the hierarchical $CoMn_2O_4$ nanowires with a high Brunauer–Emmett–Teller (BET) surface area of 70 m^2 g^{-1}, which offers a sufficient interface to facilitate the electrochemical reactions with respect to the bulk materials. A representative high-resolution TEM (HRTEM) image is shown in Fig. 3d, where a distinct set of visible lattice fringes with an inter-planar spacing of 0.49 nm can be clearly observed, corresponding to the (101) planes of $CoMn_2O_4$ crystals. Meanwhile, from the FESEM image in Fig. 3e, the sheet-like morphology of CMO-50 is perfectly retained after the thermal conversion to obtain the hierarchical $MnCo_2O_4$ nanosheets with a negligible change in size. A more interesting feature is observed from the high-magnification FESEM image (Fig. 3f). Specifically, the surface of the product becomes rather rough, indicating the formation of pores during the calcination process, which is further confirmed by TEM examination. Nonetheless, these porous structures only exhibit a relatively low BET surface of about 19 m^2 g^{-1}, due to the

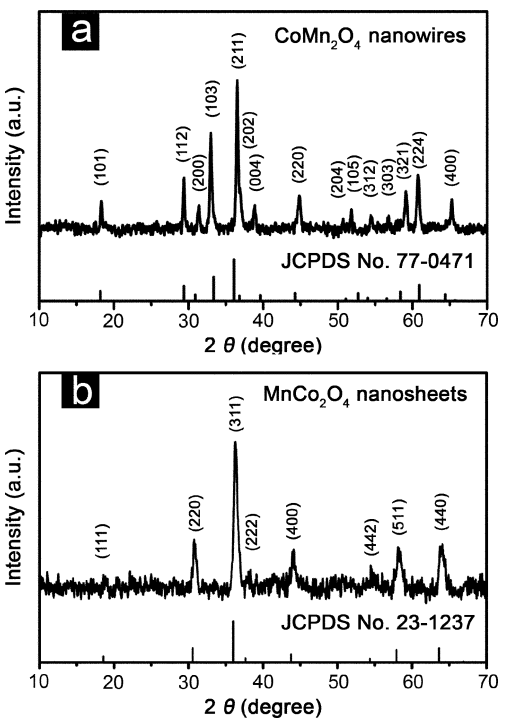

Fig. 2 XRD patterns of (a) hierarchical $CoMn_2O_4$ nanowires (from CMO-0) and (b) $MnCo_2O_4$ nanosheets (from CMO-50) scratched from stainless steel foil.

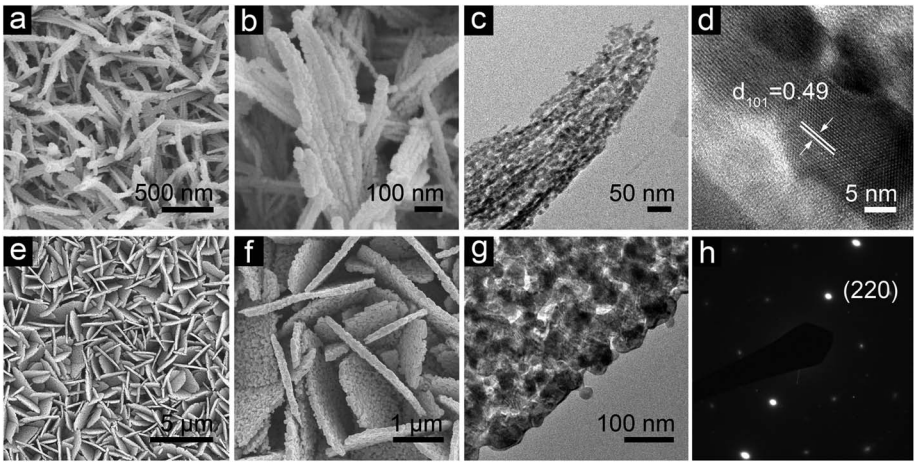

Fig. 3 FESEM and TEM characterization of a crystallized $CoMn_2O_4$ nanowire array and $MnCo_2O_4$ nanosheet array grown on stainless steel foil: (a) top view and (b) enlarged view of a nanowire array; (c) TEM image of an individual crystallized $CoMn_2O_4$ nanowire. (d) Lattice fringes from the nanowire. (e and f) FESEM images of a hierarchical $MnCo_2O_4$ nanosheet array. (g) TEM image of a $MnCo_2O_4$ nanosheet and (h) the corresponding SEAD pattern.

relatively large size of the primary nanoparticles in the porous $MnCo_2O_4$ nanosheets. The selected-area electron diffraction (SAED) pattern viewed along the $\langle 1\bar{1}1\rangle$ zone axis (Fig. 3h) reveals the single-crystal nature. This suggests that the synthesized nanosheets are exposed on the top and bottom surfaces with nominal (220) facets.

Electrochemical evaluation

It is well known that the electrochemical performance is not only dependent on the intrinsic crystalline texture and surface properties, but also greatly related to the morphology and assembled structure of active materials. Apparently, the formation of dense arrays with tunable morphology is important to the electrochemical performance of the hierarchical $Co_xMn_{3-x}O_4$ micro-/nanostructures. The direct growth of well-separated hierarchical porous microstructures of wires or sheets on conductive substrates could ensure robust mechanical adhesion and more importantly good electrical contact with the current collector in such additive-free integrated electrodes. The as-formed stable 3D framework exhibits loose texture and abundant open space to guarantee fast Li^+ ion flux across the interface. In other words, these hierarchical structures are advantageous for efficient contact between the surface of electroactive materials and the electrolyte even at high rates. On the other hand, open and porous frameworks could better improve the electrode stability by effectively mitigating the internal mechanical stress during repeated charging–discharging processes, as well as preventing the nanostructures from agglomeration. At the same time, the electrodes composed of numerous nanosized crystallites will have reduced Li^+ ion diffusion length, which also greatly enhances the electrochemical kinetics.

Motivated by these interesting structural features, we have evaluated the electrochemical lithium storage properties of hierarchical $Co_xMn_{3-x}O_4$ structures for their potential applications as additive-free integrated electrodes in LIBs. With a cut-off voltage window of 0.05–3.0 V, the representative galvanostatic discharge–charge voltage profiles of the hierarchical $CoMn_2O_4$ nanowires at a current density of 100 mA g^{-1} are shown in Fig. 4a. It is interesting that the as-synthesized hierarchical $CoMn_2O_4$ nanowires exhibit very high initial discharge and charge capacities of 1560 mA h g^{-1} and 900 mA h g^{-1}, respectively, both of which are much higher than the theoretical storage capacity (691 mA h g^{-1}). There are generally two plausible causes for this discrepancy. First, the excess discharge (Li^+ insertion) capacity could be associated with the initial formation of the solid–electrolyte interface (SEI) layer generated from electrolyte degradation, which is very common in many binary or ternary metal oxides based anodes especially when the discharge voltage goes below 1 V *vs.* Li^+/Li.[26,39–41] Such SEI films could be partly decomposed during the charge step, contributing to the charge capacity. Moreover, further oxidation of MnO to Mn_3O_4 or even Mn_2O_3 may also contribute to the total charge capacity, as observed in Kim's report on $ZnMn_2O_4$ nanowires.[42] Hence, the large irreversible capacity loss in the first cycle is mainly attributed to the incomplete decomposition of the as-formed SEI film. To further study the mechanism of lithium storage in hierarchical $CoMn_2O_4$ nanowires, differential capacity *vs.* voltage curves obtained at various cycles (Fig. 4b) are carefully investigated. During the discharge process in the first cycle, two pronounced cathodic peaks at 0.5 V and 0.9 V are observed, corresponding to the formation of metallic Mn and Co nanocrystals from MnO_x and CoO_x, respectively.[14,43] The slight shift of these two cathodic peaks to higher potentials in the following cycles might be related to some activation process caused by the Li^+ insertion in the first cycle, as observed in previous reports.[5,14,31,36] This means that the reduction becomes slightly easier in the subsequent cycles after the activation in the first cycle. Besides, an additional reduction peak centered at about 1.2 V appears ever since the second cycle, which may be related to the reduction of Mn^{3+} to Mn^{2+}.[44] This extra electrochemical activity is possibly due to the enhanced kinetics of the nanowire electrode, giving additional contribution to the total

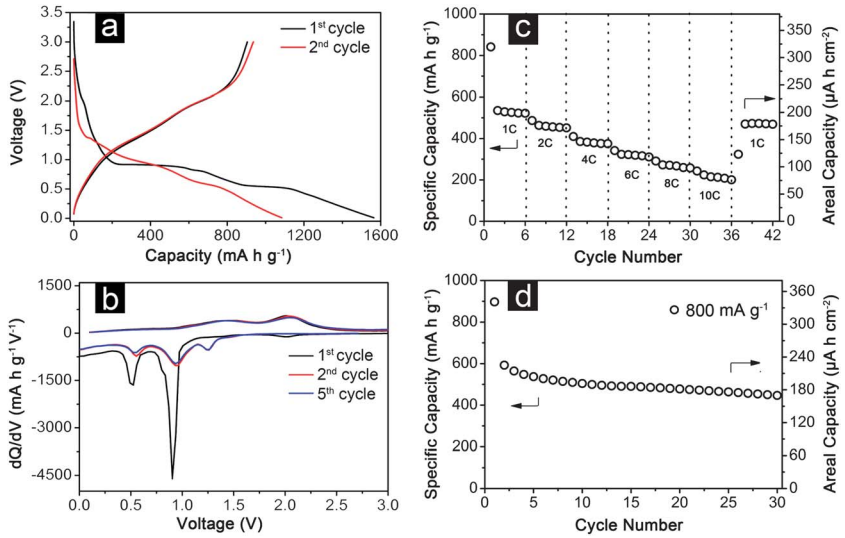

Fig. 4 Electrochemical properties of a hierarchical $CoMn_2O_4$ nanowire array grown on stainless steel foil: (a) galvanostatic discharge–charge voltage profiles for the first and second cycles; (b) differential capacity *versus* voltage plots for the 1st, 2nd and 5th cycles; (c) discharge capacity at different current rates; and (d) cycling performance at a charge–discharge current density of 800 mA g^{-1}. All measurements were conducted in the voltage range of 0.05–3.0 V.

reversible capacity. There are two oxidation peaks with good reproducibility in the Li^+ ion extraction process: the one at about 1.4 V is due to the oxidation of Mn nanocrystals to MnO_x and the other one at 2.00 V is caused by the formation of CoO_x from metallic Co nanocrystals. The introduction of Mn species with a lower lithium extraction potential would reduce the average voltage of the $Co_xMn_{3-x}O_4$ electrodes, thus increasing the output voltage of a LIB full cell. Owing to the unique structure, the hierarchical nanowires manifest excellent capacity retention at continuously varying current densities. Galvanostatic charging–discharging measurements (Fig. 4c) demonstrate that the $CoMn_2O_4$ nanowires on stainless steel can be reversibly cycled at 1–10 C (1 C = 700 mA g^{-1}), with remarkable retained capacities of 530–215 mA h g^{-1}. To evaluate the cycling stability, the $CoMn_2O_4$ nanowire-based electrode is charged and discharged at a current density of 800 mA g^{-1} over the voltage range 0.01–3.0 V, as depicted in Fig. 4d. Despite the relatively large capacity loss in the second cycle, the electrode shows good capacity retention from the second cycle onwards and eventually delivers a reversible capacity of about 450 mA h g^{-1} after 30 cycles, corresponding to 75.4% of the second cycle discharge capacity. The areal capacity of the hierarchical nanowires is also displayed by the vertical axis on the right in Fig. 4d, where it decreases gradually to about 171 μA h cm^{-1} after 30 cycles. To the best of our knowledge, this might be the first report on utilizing $CoMn_2O_4$ nanostructures as integrated electrodes for LIBs. Considering that no ancillary additives such as polymer binder and carbon black are employed in the electrode, the reversible rate capability and cycling stability presented above for the hierarchical nanowire arrays are highly attractive compared to previously reported $CoMn_2O_4$ electrodes.[14–16,18,19,44]

With hierarchical $MnCo_2O_4$ nanosheets, the structural advantages are proved once again in terms of remarkable electrochemical performance. As shown in Fig. 5a and b, the discharge process of these $MnCo_2O_4$ nanosheets is quite different with that in the $CoMn_2O_4$ nanowire electrode (Fig. 4a and b). Specifically, there is only one major cathodic peak observed at around 0.8 V in the first cycle and 0.9–1.0 V in the subsequent cycles. Also there is no distinct peak related to the Mn^{2+}/Mn^{3+} redox couple observed in the differential curves (Fig. 5b). The exact reason for the differences observed in the electrochemical behaviour of the two electrodes appears unclear at this point. From the rate capability test shown in Fig. 5c, the average specific capacities of hierarchical $MnCo_2O_4$ nanosheets are 540, 455, 380, 340 and 305 mA h g^{-1} at the current densities of 1 C, 2 C, 4 C, 6 C, and 8 C, respectively (1 C = 700 mA g^{-1}). At a very high rate of 10 C, the specific charge capacity is still retained as 270 mA h g^{-1}. Moreover, the capacity could return to almost the original value of 530 mA h g^{-1} when the current rate is reduced back to 1 C, which indicates the good reversibility of the electrode materials. In addition, the hierarchical $MnCo_2O_4$ nanosheets possess excellent cycling performance even at a higher current density of 800 mA g^{-1}, with a capacity retention of 460 mA h g^{-1} after 30 cycles (Fig. 5d).

In order to further understand the enhanced lithium storage performance of $Co_xMn_{3-x}O_4$ samples, electrochemical impedance measurements are carried out before and after charge–discharge experiments (Fig. S9, see the ESI†). It is obvious that the samples have lower charge-transfer impedance after discharging and recharging for 10 cycles at 800 mA g^{-1} than that of the fresh cells, which might be ascribed to the activation and reconstruction of the $Co_xMn_{3-x}O_4$ structures in the first few cycles. It is also noteworthy that the charge-transfer impedance of $MnCo_2O_4$ nanosheets is always lower than that of $CoMn_2O_4$ nanowires, which might result in the enhanced electrode reaction kinetics and better cycling performance. More importantly, after charging–discharging for 10 cycles at 800 mA g^{-1} (Fig. S10, see the ESI†), the morphologies and structures of the $Co_xMn_{3-x}O_4$ samples can be generally retained with slight

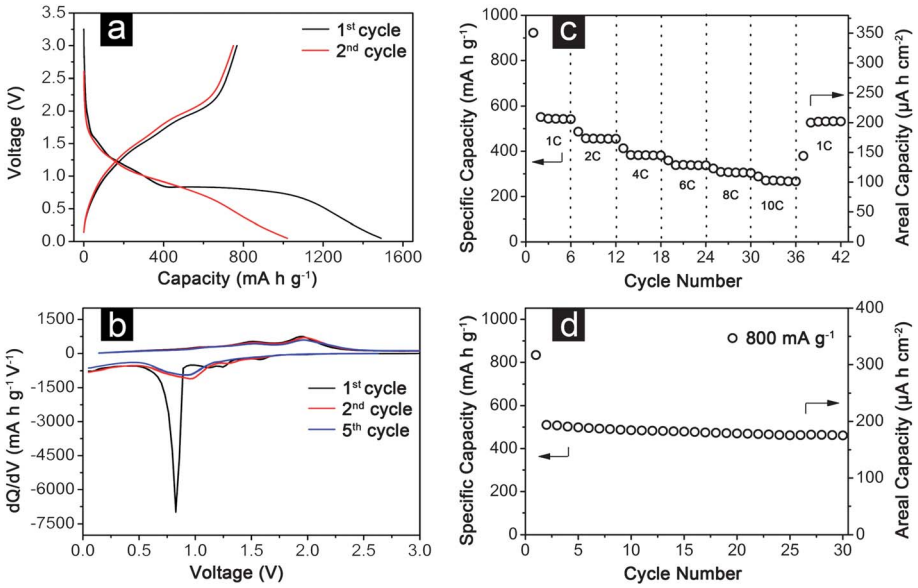

Fig. 5 Electrochemical properties of a hierarchical $MnCo_2O_4$ nanosheet array grown on stainless steel foil: (a) galvanostatic discharge–charge voltage profiles for the first and second cycles; (b) differential capacity *versus* voltage plots for the 1st, 2nd and 5th cycles; (c) discharge capacity at different current rates; (d) cycling performance at a charge–discharge current density of 800 mA g^{-1}. All measurements were conducted in the voltage range of 0.05–3.0 V.

aggregation observed. This observation is a good demonstration of the bulk structural stability of $Co_xMn_{3-x}O_4$ micro-/nanostructures, and thus leading to enhanced cycling stability.

Evidently, owing to their unique structural features, the hierarchical $Co_xMn_{3-x}O_4$ micro-/nanostructures grown on conductive substrates have been shown to exhibit interesting properties as potential integrated electrodes for LIBs. Lastly, it should be pointed out that it is very challenging to calculate accurately the specific capacity due to the uncertainty associated with weighing a small amount of active materials on the substrate.

Conclusions

In summary, we have developed a facile strategy for the preparation of morphology-controlled hierarchical $Co_xMn_{3-x}O_4$ micro-/nanostructures with tunable compositions on the stainless steel substrate. The strategy involves the growth of precursor structures and subsequent thermal conversion. The structure can be easily controlled by using a simple ethanol–water mixed solvent with different volume ratios. The hierarchical $Co_xMn_{3-x}O_4$ structures exhibit interesting electrochemical performance as integrated electrodes for lithium-ion batteries. The specific capacities are in the range of 540–207 mA h g^{-1} at various current rates of 1–10 C. These integrated functional materials may hold great promise for the construction of advanced electrodes for high performance energy storage devices.

References

1 P. G. Bruce, B. Scrosati and J. M. Tarascon, *Angew. Chem., Int. Ed.*, 2008, **47**, 2930.
2 J. B. Goodenough and Y. Kim, *Chem. Mater.*, 2010, **22**, 587.
3 V. Etacheri, R. Marom, R. Elazari, G. Salitra and D. Aurbach, *Energy Environ. Sci.*, 2011, **4**, 3243.
4 P. G. Bruce, S. A. Freunberger, L. J. Hardwick and J. M. Tarascon, *Nat. Mater.*, 2012, **11**, 19.
5 Z. Y. Wang, L. Zhou and X. W. Lou, *Adv. Mater.*, 2012, **24**, 1903.
6 F. Y. Cheng, J. Liang, Z. L. Tao and J. Chen, *Adv. Mater.*, 2011, **23**, 1695.
7 H. Q. Li and H. S. Zhou, *Chem. Commun.*, 2012, **48**, 1201.
8 Y. Li, Z. Y. Fu and B. L. Su, *Adv. Funct. Mater.*, 2012, **22**, 4634.
9 A. S. Arico, P. Bruce, B. Scrosati, J. M. Tarascon and W. Van Schalkwijk, *Nat. Mater.*, 2005, **4**, 366.
10 N. S. Choi, Z. H. Chen, S. A. Freunberger, X. L. Ji, Y. K. Sun, K. Amine, G. Yushin, L. F. Nazar, J. Cho and P. G. Bruce, *Angew. Chem., Int. Ed.*, 2012, **51**, 9994.
11 J. B. Goodenough and K. S. Park, *J. Am. Chem. Soc.*, 2013, **135**, 1167.
12 L. W. Ji, Z. Lin, M. Alcoutlabi and X. W. Zhang, *Energy Environ. Sci.*, 2011, **4**, 2682.
13 F. M. Courtel, H. Duncan, Y. Abu-Lebdeh and I. J. Davidson, *J. Mater. Chem.*, 2011, **21**, 10206.
14 L. Zhou, D. Y. Zhao and X. W. Lou, *Adv. Mater.*, 2012, **24**, 745.
15 L. Hu, P. Zhang, H. Zhong, X. R. Zheng, N. Yan and Q. W. Chen, *Chem.–Eur. J.*, 2012, **18**, 15049.
16 J. F. Li, S. L. Xiong, X. W. Li and Y. T. Qian, *J. Mater. Chem.*, 2012, **22**, 23254.
17 J. F. Li, S. L. Xiong, X. W. Li and Y. T. Qian, *Nanoscale*, 2013, **5**, 2045.
18 L. J. Wang, B. Liu, S. H. Ran, L. M. Wang, L. N. Gao, F. Y. Qu, D. Chen and G. Z. Shen, *J. Mater. Chem. A*, 2013, **1**, 2139.
19 L. Hu, H. Zhong, X. R. Zheng, Y. M. Huang, P. Zhang and Q. W. Chen, *Sci. Rep.*, 2012, **2**, 986.
20 W. Y. Li, L. N. Xu and J. Chen, *Adv. Funct. Mater.*, 2005, **15**, 851.
21 S. L. Xiong, J. S. Chen, X. W. Lou and H. C. Zeng, *Adv. Funct. Mater.*, 2012, **22**, 861.

22 G. Q. Zhang, L. Yu, H. B. Wu, H. E. Hoster and X. W. Lou, *Adv. Mater.*, 2012, **24**, 4609.
23 H. L. Wang, L. F. Cui, Y. A. Yang, H. S. Casalongue, J. T. Robinson, Y. Y. Liang, Y. Cui and H. J. Dai, *J. Am. Chem. Soc.*, 2010, **132**, 13978.
24 L. F. Hu, L. M. Wu, M. Y. Liao, X. H. Hu and X. S. Fang, *Adv. Funct. Mater.*, 2012, **22**, 998.
25 B. Liu, J. Zhang, X. F. Wang, G. Chen, D. Chen, C. W. Zhou and G. Z. Shen, *Nano Lett.*, 2012, **12**, 3005.
26 Z. Y. Wang, Z. C. Wang, W. T. Liu, W. Xiao and X. W. Lou, *Energy Environ. Sci.*, 2013, **6**, 87.
27 P. Poizot, S. Laruelle, S. Grugeon, L. Dupont and J. M. Tarascon, *Nature*, 2000, **407**, 496.
28 Y. Wang and G. Z. Cao, *Adv. Mater.*, 2008, **20**, 2251.
29 Y. G. Guo, J. S. Hu and L. J. Wan, *Adv. Mater.*, 2008, **20**, 2878.
30 H. B. Wu, J. S. Chen, H. H. Hng and X. W. Lou, *Nanoscale*, 2012, **4**, 2526.
31 G. N. Zhu, Y. G. Wang and Y. Y. Xia, *Energy Environ. Sci.*, 2012, **5**, 6652.
32 X. W. Lou, L. A. Archer and Z. C. Yang, *Adv. Mater.*, 2008, **20**, 3987.
33 I. Lahiri, S. W. Oh, J. Y. Hwang, S. Cho, Y. K. Sun, R. Banerjee and W. Choi, *ACS Nano*, 2010, **4**, 3440.
34 L. Taberna, S. Mitra, P. Poizot, P. Simon and J. M. Tarascon, *Nat. Mater.*, 2006, **5**, 567.
35 M. M. Shaijumon, E. Perre, B. Daffos, P. L. Taberna, J. M. Tarascon and P. Simon, *Adv. Mater.*, 2010, **22**, 4978.
36 J. Jiang, Y. Y. Li, J. P. Liu, X. T. Huang, C. Z. Yuan and X. W. Lou, *Adv. Mater.*, 2012, **24**, 5166.
37 L. F. Shen, E. Uchaker, X. G. Zhang and G. Z. Cao, *Adv. Mater.*, 2012, **24**, 6502.
38 L. Yu, Z. Y. Wang, L. Zhang, H. B. Wu and X. W. Lou, *J. Mater. Chem. A*, 2013, **1**, 122.
39 Z. S. Wu, W. C. Ren, L. Wen, L. B. Gao, J. P. Zhao, Z. P. Chen, G. M. Zhou, F. Li and H. M. Cheng, *ACS Nano*, 2010, **4**, 3187.
40 M. V. Reddy, T. Yu, C. H. Sow, Z. X. Shen, C. T. Lim, G. V. S. Rao and B. V. R. Chowdari, *Adv. Funct. Mater.*, 2007, **17**, 2792.
41 Y. Sharma, N. Sharma, G. V. S. Rao and B. V. R. Chowdari, *Adv. Funct. Mater.*, 2007, **17**, 2855.
42 S. W. Kim, H. W. Lee, P. Muralidharan, D. H. Seo, W. S. Yoon, D. K. Kim and K. Kang, *Nano Res.*, 2011, **4**, 505.
43 Z. Y. Wang, D. Y. Luan, S. Madhavi, Y. Hu and X. W. Lou, *Energy Environ. Sci.*, 2012, **5**, 5252.
44 H. W. Liu and J. Wang, *J. Electron. Mater.*, 2012, **41**, 3107.